ACS APPLIED MATERIALS & INTERFACES

www.acsami.org

Research Article

Engineering the Electronic, Thermoelectric, and Excitonic Properties of Two-Dimensional Group-III Nitrides through Alloying for Optoelectronic Devices ($B_{1-x}Al_xN$, $Al_{1-x}Ga_xN$, and $Ga_{1-x}In_xN$)

Daniel Wines, Fatih Ersan, and Can Ataca*

Cite This: *ACS Appl. Mater. Interfaces* 2020, 12, 46416−46428

Read Online

ACCESS | Metrics & More | Article Recommendations | Supporting Information

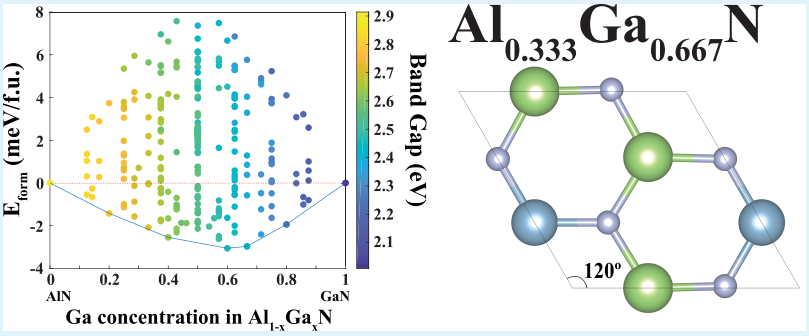

ABSTRACT: Recently, two-dimensional (2D) group-III nitride semiconductors such as h-BN, h-AlN, h-GaN, and h-InN have attracted attention because of their exceptional electronic, optical, and thermoelectric properties. It has also been demonstrated, theoretically and experimentally, that properties of 2D materials can be controlled by alloying. In this study, we performed density functional theory (DFT) calculations to investigate 2D $B_{1-x}Al_xN$, $Al_{1-x}Ga_xN$, and $Ga_{1-x}In_xN$ alloyed structures. We also calculated the thermoelectric properties of these structures using Boltzmann transport theory based on DFT and the optical properties using the GW method and the Bethe−Salpeter equation. We find that by changing the alloying concentration, the band gap and exciton binding energies of each structure can be tuned accordingly, and for certain concentrations, a high thermoelectric performance is reported with strong dependence on the effective mass of the given alloyed monolayer. In addition, the contribution of each e−h pair is explained by investigating the e−h coupling strength projected on the electronic band structure, and we find that the exciton binding energy decreases with increase in sequential alloying concentration. With the ability to control such properties by alloying 2D group-III nitrides, we believe that this work will play a crucial role for experimentalists and manufacturers focusing on next-generation electronic, optoelectronic, and thermoelectric devices.

KEYWORDS: *2D materials, alloys, group-III nitrides, density functional theory, GW approximation, optoelectronic, thermoelectric, excitonic*

INTRODUCTION

Group-III nitrides[1] represent a family of semiconducting materials with a tunable band gap that spans from the infrared to ultraviolet, making them ideal candidates for optoelectronic devices.[2,3] Since the synthesis and extensive study of graphene,[4] research has been focused on the theoretical and experimental investigation of other two-dimensional (2D) materials. In addition to monolayer group-III nitrides such as AlN, BN, GaN, and InN having previously been theoretically predicted,[5−7] AlN and GaN nanosheets and BN monolayers have been experimentally realized.[8−11] The graphene-like planar honeycomb structures such as h-BN, h-AlN, h-GaN, and h-InN have been rigorously studied, and exceptional electronic, optical, and thermoelectric properties have been revealed.[12−15] In addition to the intrinsic characteristics of group-III nitride monolayers, it has been demonstrated that the electronic properties of these materials can be tuned for specific applications such as photovoltaics by creating heterostructures.[16−19] Theoretical studies also indicate that for h-BN, h-GaN, and h-AlN, applied biaxial strain can induce indirect to direct band gap transitions and alter the band gap value,[15] and full or semihydrogenation causes h-GaN and h-AlN to retain their nonmagnetic semiconducting properties.[20]

Alloying is a promising route to control the electronic properties of a given material for specific applications. This

Received: June 18, 2020
Accepted: September 18, 2020
Published: September 18, 2020

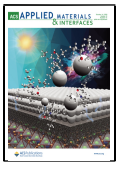

https://dx.doi.org/10.1021/acsami.0c11124
ACS Appl. Mater. Interfaces 2020, 12, 46416−46428

approach has been used for bulk materials including group-III semiconductors, where the electronic properties of bulk $B_xAl_{1-x}N$ alloys have theoretically been controlled with constituent composition.[21] With regard to 2D materials, it has been shown through experiment and density functional theory (DFT) that the electronic properties of these structures can change significantly and peculiar effects can be induced in their electronic structures.[22−27] For example, DFT has revealed that the structural and electronic properties of monolayer $TiX_{3(1-x)}X'_{3x}$ alloys (where X and X′ = Se and Te) are dependent on chalcogen composition.[26] More specifically, the substitutional doping of Te atoms into TiS_3 or $TiSe_3$ monolayers results in a semiconductor to metal transition.[26] DFT studies also indicate that varying the concentration of monolayer $MoS_{2(1-x)}Se_{2x}$ alloys can affect the adsorption and diffusion of lithium in the structure[27] and that 2D pnictogen alloys can be used as effective anode materials for batteries.[28] Experimentally, it has been reported that when GaSe nanostructures are alloyed with Te (to create $GaSe_{1-x}Te_x$), the structures undergo a hexagonal to monoclinic transition and there exists an instability region where both phases compete and two different band gap values can be found at the same composition, leading to anomalous band bowing effects.[24] In addition, experimentally, the photoresponse of 2D $Mo_{1-x}Sn_xS_2$ can effectively be tuned by varying composition[29] and the polarization photodetection can be enhanced by alloying $Nb_{1-x}Ti_xS_3$.[25]

More recently, it has been demonstrated through first-principles calculations that the electronic properties of low-dimensional group-III nitride alloys such as $In_xGa_{1-x}N$[22] and $Ga_{1-x}Al_xN$[23] can change by varying composition. Specifically, it has been reported that increasing the Al concentration in monolayer $Ga_{1-x}Al_xN$ increases the band gap and in plane stiffness and blue-shifts the dielectric function at the DFT level.[23] Also, it has been reported that increasing the Ga concentration in bilayer and trilayer $In_xGa_{1-x}N$ results in an increase in lattice constant and a decrease in band gap.[22]

Because of their reduced dimensionality, 2D materials experience a reduced level of screening. Stemming from this reduced screening are peculiar optical properties, including the presence of bound electron−hole pairs (excitons) and increased absorbance in the visible light and infrared ranges.[30] These optical properties and excitonic effects have been extensively studied experimentally and theoretically [using many-body perturbation theory (GW approximation) and solving the Bethe−Salpeter equation (BSE)] in 2D structures such as graphene and transition metal dichalcogenides (TMDs).[31,32] In addition to electronic properties, optical properties (including excitonic effects) can be tuned by alloying.[25,26,33,34] For example, TMD alloys such as $Mo_xW_{1-x}S_2$ structures with certain W concentrations can have bright excitons, while other concentrations yield dark excitons.[33,34] Additionally, tunable excitonic effects have been reported for monolayer BN-encapsulated $WS_{2x}Se_{2(1-x)}$.[35] Because of these interesting optical phenomena, these 2D materials have potential applications such as photovoltaic solar cells, photodetectors, and light-emitting diodes.[32,36] Previously, bulk group-III nitride structures such as h-BN have been investigated experimentally and using the GW-BSE framework where large exciton binding energies have been revealed.[37] First-principles calculations also revealed strong excitonic effects in group-III monolayers such as AlN, GaN, BN, and InN.[38]

Another important property emerging in today's material research (in bulk and monolayer forms) is thermoelectricity. Thermoelectric (TE) materials are important because of their ability to convert heat into electricity in a clean manner.[39] The efficiency of a TE material is defined by its dimensionless figure of merit $ZT = S^2\sigma T/\kappa$ where T is the absolute temperature, S is the Seebeck coefficient, σ is the electrical conductivity, and κ is the thermal conductivity (which consists of the lattice thermal conductivity and the electronic thermal conductivity).[39] In order to obtain a high value for ZT, a high value of power factor (PF), defined as σS^2, is required. Candidate materials for TE power must be chemically and thermally stable materials at high temperature. It has been revealed, experimentally and theoretically, that group-III nitride semiconductors and their alloys are good candidates for TE devices in their bulk form.[40,41] Recently, the TE properties of 2D group-III nitride materials such as AlN, GaN, and BN have been investigated from first-principles.[15,42] Other theoretical[43] and experimental[44] studies have demonstrated that alloying TE materials can change TE properties.[43,44] Specifically, alloying CoAsS with Sb can result in an 8−11% increase in the figure of merit value, and alloying InSb with Ga can result in a 46% reduction in thermal conductivity.[43,44]

In this study, we generated 2D $B_{1-x}Al_xN$, $Al_{1-x}Ga_xN$, and $Ga_{1-x}In_xN$ alloyed structures using the first-principles special quasirandom structure (SQS) method,[45] which has been used extensively to study alloy systems,[46,47] to search for possible energetically stable ground-state configurations. We observe that $Al_{1-x}Ga_xN$ can have thermodynamically stable ground-state configurations at x = 0.2, 0.4, 0.6, 0.667, and 0.8 and $Ga_{1-x}In_xN$ can have configurations at x = 0.333 and 0.667 (where x is the alloying concentration). For $B_{1-x}Al_xN$, we do not observe any possible energetically stable ground states for $x \neq 0$ or 1. We further examine the geometric and electronic properties of these ground-state configurations and compare them to monolayer h-BN, h-AlN, h-GaN, and h-InN. It is found that increasing the alloying concentration in $Al_{1-x}Ga_xN$ and $Ga_{1-x}In_xN$ results in a decrease in band gap value, proving that alloying 2D group-III nitride materials is an effective way to tune the band gap. We also calculated the optical properties, including the frequency-dependent dielectric function and the exciton binding energy, using the GW-BSE method. We find that these materials exhibit strongly bound excitons and that changing the alloying concentration can effectively change the exciton binding energy in the 2D group-III nitride alloyed material. Finally, we calculated the thermoelectric properties of these structures using Boltzmann transport theory and found that certain structures exhibit high thermoelectric performance under certain conditions with a strong dependence on the effective mass. To further quantify our thermoelectric results, we calculated the effective charge carrier mass and relaxation time for each structure. These desirable properties and the ability to engineer these properties through alloying make these materials ideal for device applications in the electronic, thermoelectric, and optoelectronic industries. Specifically, these materials can be used in UV polaritonic applications, exhibit electrically driven excitonic light emission, and can be used as photodetectors, photovoltaic solar cells, valley-optoelectronic devices, and thermoelectric power conversion.

COMPUTATIONAL DETAILS

Our results were obtained from first-principles based on DFT within the generalized gradient approximation (GGA).

https://dx.doi.org/10.1021/acsami.0c11124
ACS Appl. Mater. Interfaces 2020, 12, 46416−46428

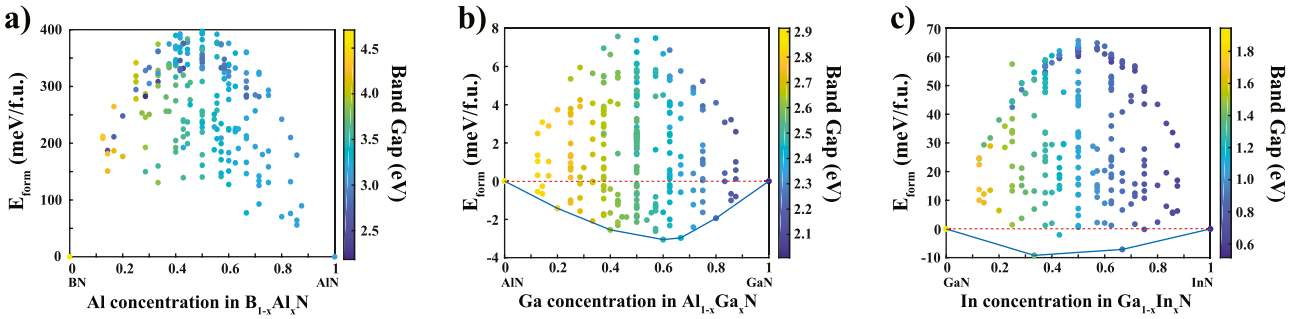

Figure 1. Formation energy (in eV/formula unit) as a function of concentration for the (a) $B_{1-x}Al_xN$, (b) $Al_{1-x}Ga_xN$, and (c) $Ga_{1-x}In_xN$ alloys created with the SQS method. Each data point represents a different structure, and the color axis indicates the band gap value (calculated with the PBE functional) for each structure. The blue line at the bottom of (b,c) represents the ground-state configurations of these alloys (convex hull).

Projected augmented-wave potentials were used, the exchange−correlation functional was approximated with the Perdew−Burke−Ernzerhof (PBE) functional, and van der Waals effects were included using the DFT-D2 method.[48−50] The kinetic energy cutoff of the plane-wave basis set was taken to be 475 eV, and the Monkhorst-Pack scheme was used to sample the Brillouin zone (BZ).[51] A 20 × 20 × 1 mesh in $\vec{k}$ space was used for 2D structures in the primitive cell and scaled accordingly for larger supercells. The numerical calculations were carried out using the Vienna Ab initio Simulation Package code.[52] The atomic positions of each structure were optimized using the conjugate gradient method, where the total energy and forces were minimized. For this optimization, a maximum force of 0.002 eV/Å was allowed on each atom, and the energy convergence between two consecutive steps was set to 10^{-5} eV. The Gaussian-type Fermi level smearing method was used with a smearing width of 0.01 eV and was increased to 0.05 eV for total and orbital projected density of states calculations. The vacuum spacing between periodic layers was set to 20 Å to minimize any interlayer coupling. Because fundamental band gaps are underestimated using PBE functionals, we performed calculations with the hybrid functional HSE06, which is formed by mixing 75% of the PBE exchange with 25% of the Fock exchange and 100% of the correlation energy from PBE.[53] We also calculated band gaps with the recently developed nonempirical strongly constrained and appropriately normed (SCAN) *meta*-GGA[54] functional (without vdW corrections), which has been shown to yield more accurate results than standard PBE and at a smaller computational cost than HSE06.

To generate $B_{1-x}Al_xN$, $Al_{1-x}Ga_xN$, and $Ga_{1-x}In_xN$ alloyed structures with varying concentrations, the SQS method was used as implemented in the ATAT package.[45,55] The formation energy E_{form} (in eV/f.u.) of $X_{1-x}Y_xN$ (where X and Y = B, Al, Ga, and In) is defined as $E_{form} = (E_{X_{1-x}Y_xN} - (1 - x)E_{XN} - xE_{YN})$, where $E_{X_{1-x}Y_xN}$ is the energy of an $X_{1-x}Y_xN$ cell, E_{XN} is the energy of an XN cell, and E_{YN} is the energy of a YN cell, all per formula unit. In the ATAT code, the energies of these randomly created structures are used as a training set to calculate fitted energies. When the calculated and fitted energies match within a convergence criteria known as the cross validation score (which is specifically designed to estimate the error made in predicting the energy for structures and analogous to the root mean square error), we know that we have a large enough training set of randomly generated structures and can verify our predictions. In our calculations, we set the minimum cross validation score to 25 meV (which ATAT recommends[45,55]) for the training set of each alloy series. Once the cross validation score is beneath this threshold, we can say with confidence that the structures with the lowest formation energy can be energetically stable at 0 K. In contrast to previous studies involving monolayer $In_xGa_{1-x}N$[22] and $Ga_{1-x}Al_xN$,[23] we considered very large training sets (~200 structures per alloy series) in order to screen the most probable ground-state alloyed structures. Bader charge analysis[56] was used to obtain the charge distribution on the atoms in the cell.

To obtain accurate quasiparticle band gaps and the frequency-dependent dielectric function, including electron−electron and electron−hole interactions, we employed the GW method[57,58] and the BSE.[59] We applied the GW method perturbatively, using the G_0W_0 ("single shot") method, to obtain first-order corrections to the Kohn−Sham eigenvalues and wave functions obtained from DFT to use as a starting point for the BSE. For all GW and BSE calculations, we used a k-point grid of 9 × 9 × 1 and a number of empty bands that were at least 10 times the number of electrons in the simulation cell. For the BSE calculations, the Tamm−Dancoff approximation[60] with 24 occupied and unoccupied bands was used. We calculated the thermoelectric properties based on DFT (PBE) and Boltzmann transport theory using the BoltzTraP2 code, which uses the rigid band approach to calculate the transport coefficients.[61] Because our band gaps are also obtained with accurate G_0W_0 simulations, we performed a scissor operation in BoltzTraP2 to shift the PBE band gap to our G_0W_0 gap to calculate electronic transport quantities. Because of the fact that results with BoltzTraP2 are calculated with respect to constant relaxation time, a more rigorous treatment of the relaxation time is needed to adequately describe these transport quantities. To calculate relaxation time, we used an analytical model based on deformation potential theory (DPT)[62] based on the effective mass approximation. Expanded methodology of our thermoelectric calculations is given in the Supporting Information.

RESULTS AND DISCUSSION

Structure Optimization and Alloying. For comparison sake, we optimized the structures of hexagonal BN, AlN, GaN, and InN with the PBE functional. Our obtained lattice parameters were $a = b = 2.50$ Å for BN, 3.11 Å for AlN, 3.24 Å for GaN, and 3.64 Å for InN which are comparable to the literature and available experimental (for BN and AlN) results.[9,12,15,38] To search for new stable group-III nitride alloys, we created three types of alloys ($B_{1-x}Al_xN$, $Al_{1-x}Ga_xN$,

https://dx.doi.org/10.1021/acsami.0c11124
ACS Appl. Mater. Interfaces 2020, 12, 46416−46428

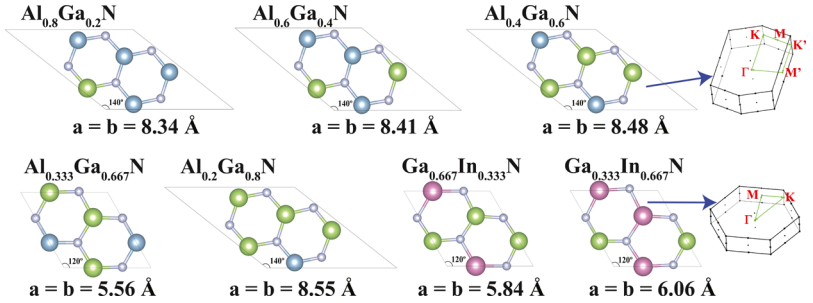

Figure 2. Geometric structures and lattice constants for the ground-state configurations of the $Al_{1-x}Ga_xN$ and $Ga_{1-x}In_xN$ alloys. A schematic of the Brillouin zone for distorted hexagonal (upper row) and hexagonal (lower row) unit cell shapes are also given. The small dark blue spheres represent N atoms, and the large light blue, green, and magenta spheres represent Al, Ga, and In atoms, respectively.

and $Ga_{1-x}In_xN$) using the SQS method and calculated the formation energy of each structure. In addition, the lattice constant and atomic positions of each created alloy were allowed to relax as the concentration was varied. The reason we only considered sequential alloys (next row elements in the periodic table) instead of all possible variations was to minimize the lattice mismatch and local strain in each alloy series. We know that as we go from BN to AlN to GaN to InN, the lattice constant increases because of the heavier/larger group-III atom, and it is logical to start from BN and introduce impurities sequentially until we reach InN.

Figure 1 depicts the formation energy (in eV/f.u.) as a function of concentration for $B_{1-x}Al_xN$, $Al_{1-x}Ga_xN$, and $Ga_{1-x}In_xN$ alloys. Each data point represents a different supercell created by SQS to preserve a specific alloying ratio. We can see that for many structures, the formation energy is negative, implying that these alloys are energetically stable and homogeneous and can form spontaneously. Alloys that have a formation energy that lie on the ground-state line [blue solid line at the bottom of Figure 1b,c, otherwise known as the convex hull] represent the ground-state configurations that are energetically stable at 0 K. For $B_{1-x}Al_xN$, there are no alloyed structures with a negative formation energy, indicating that the only stable $B_{1-x}Al_xN$ structures are for a concentration of $x = 0$ (BN) and $x = 1$ (AlN). This implies that alloys of $B_{1-x}Al_xN$ will most likely be inhomogeneous. There exists five stable ground-state structures for $Al_{1-x}Ga_xN$ at alloying concentrations of $x = 0.2$, $x = 0.4$, $x = 0.6$, $x = 0.667$, and $x = 0.8$ (different alloying concentrations), and there exists two stable ground-state structures for $Ga_{1-x}In_xN$ at $x = 0.333$ and $x = 0.667$. Our formation energy results indicate that for $Al_{1-x}Ga_xN$ structures, $Al_{0.4}Ga_{0.6}N$ is the most energetically favorable and for $Ga_{1-x}In_xN$ structures, $Ga_{0.667}In_{0.333}N$ is the most favorable. It is possible that there exist other alloys with lower formation energy if we considered a larger training set of randomly generated alloys. Because the cross validation score of each alloy series lies below 25 meV (the recommended value[45,55]), we can say with confidence that the ground states we predict are most likely the ground-state structures (or very close to ground-state concentration) that may exist in nature. To further confirm the stability of these alloys, we calculated the vibrational free energy and phonon dispersion curves of each structure with the finite-displacement method using the phonopy code.[63] We considered the vibrational free energy at 0 and 300 K and recalculated the formation energies, taking these quantities into account. These alloy formation energies (presented in Table S1) still remain negative below the convex hull at 0 and 300 K when vibrational free energy is taken into account. Additionally, none of the structures have negative frequencies in their phonon dispersion and phonon density of states, which gives further evidence that these structures are energetically stable and can form spontaneously (see Figure S1).

To further investigate the effect of alloying monolayer group-III nitrides, we examined how the geometric structure of the ground-state configurations changed with respect to alloying concentration. To model alloys at specific concentrations, the SQS method creates supercells of varying atom number and cell shape. Upon geometric optimization, some of the alloyed ground-state structures preserve their original hexagonal cell shape, while others are slightly distorted, depending on alloying concentration. For the $Al_{1-x}Ga_xN$ alloys at $x = 0.2$, $x = 0.4$, $x = 0.6$, and $x = 0.8$, the angle between the $\vec{a}$ and $\vec{b}$ vectors increased from 120° (regular hexagonal cell) to 140° (distorted hexagonal cell). For these distorted hexagonal structures (at $x = 0.2$, 0.4, 0.6, and 0.8), the lattice constant increases as Ga concentration increases, as seen in Figure 2. It is important to note that although the angle between $\vec{a}$ and $\vec{b}$ increases to 140° for the distorted hexagonal structures, the internal angles of each hexagon remain 120°, and therefore, the symmetry of the honeycomb structure is preserved. The ground-state structure $Al_{0.333}Ga_{0.667}N$ retains its original hexagonal shape and has a much smaller lattice constant of $a = b = 5.56$ Å when compared with the distorted hexagonal structures. The Brillouin zone of the original hexagonal structure and the distorted hexagonal structure for various alloys is given in Figure 2. It is important to note that these distorted hexagonal cells contain a total of ten atoms, while the original hexagonal cells contain six atoms. For the $Ga_{1-x}In_xN$ ground-state structures, the cells retain their hexagonal shape upon geometric optimization, and the lattice constants increase as In concentration increases. A full summary of bond lengths, angles between atoms, and angles between lattice vectors is given in Table S2.

Charge Transfer and Electronic Structure of Alloys. To understand the charge transfer of the group-III nitride alloys, we performed Bader charge analysis. We started by calculating the charge transfer of the nonalloyed monolayers and observed that B transfers $2.1e^-$ to N for BN, Al transfers $2.3e^-$ to N for AlN, Ga transfers $1.35e^-$ to N for GaN, and In transfers $1.2e^-$ to N for InN. This transfer of charge occurs because N has a much higher electronegativity of 3.04 than B (2.04), Al (1.61), Ga (1.81), and In (1.78), according to the Pauling scale for electronegativity. Disparities in the amount of charge transferred can be explained by the increase in lattice constant as we go down the periodic table from B to In. We

https://dx.doi.org/10.1021/acsami.0c11124
ACS Appl. Mater. Interfaces 2020, 12, 46416−46428

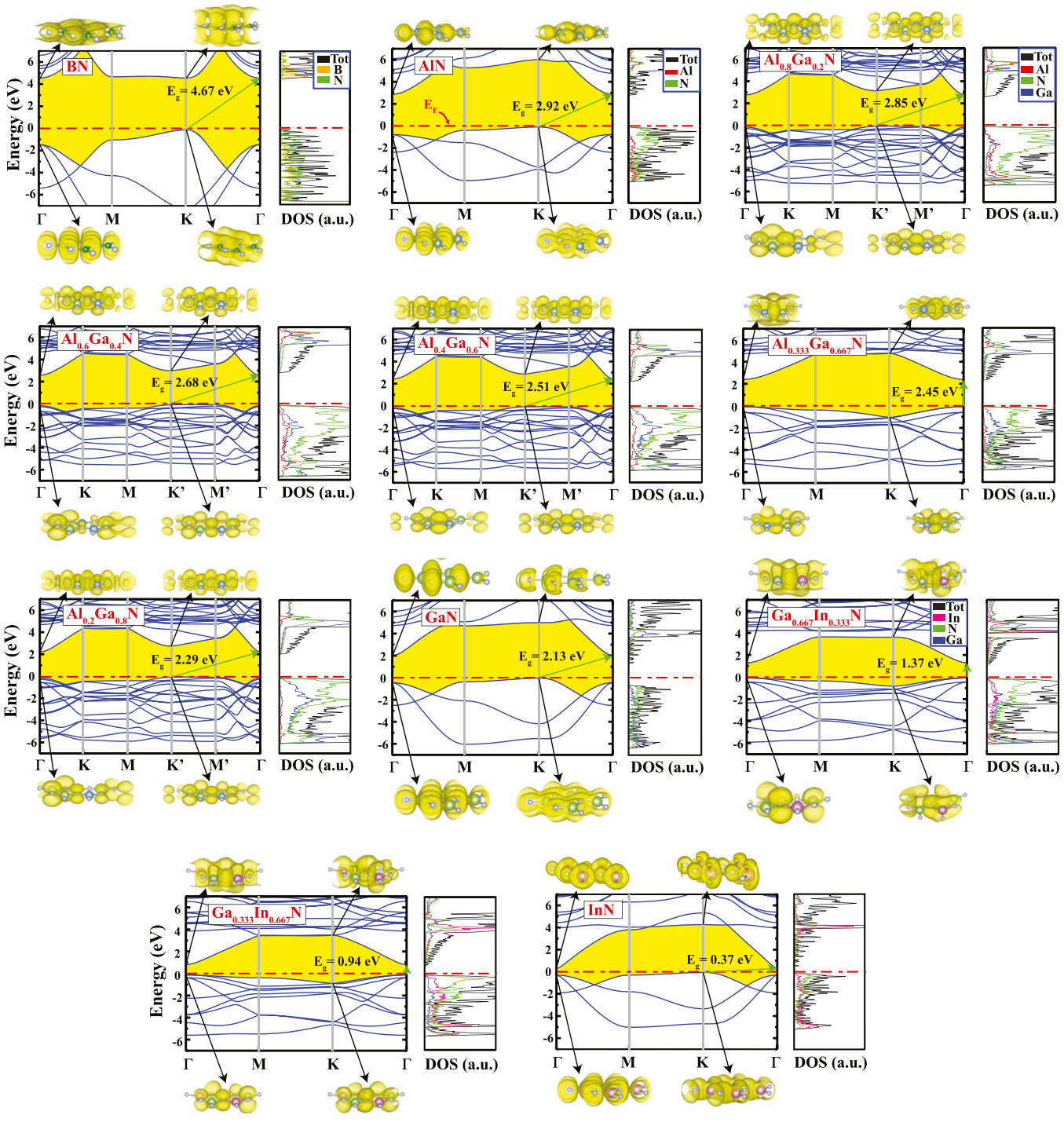

Figure 3. Electronic band structure, electronic density of states, orbital-projected density of states, and band decomposed charge densities (BDCD) of BN, AlN, GaN, and InN and the ground-state configurations of the $Al_{1-x}Ga_xN$ and $Ga_{1-x}In_xN$ alloys using the PBE functional. The red dashed line denotes the Fermi level which is set to 0 eV, and the green arrow extends from the valence band maximum (VBM) to the conduction band minimum (CBM) to illustrate the band gap of a given material, whether it is direct or indirect. The isosurface value for the BDCD was set to 1×10^{-5} e/Å^3. The PBE band gaps are also included in Table 1.

also see that when Ga is introduced into AlN, N atoms gain electrons from Ga atoms, and when In is introduced into GaN, charge is transferred from In to N, in accordance with electronegativity rules. For the distorted hexagonal $Al_{1-x}Ga_xN$ alloys, we observe an asymmetric charge distribution on the N atoms in the unit cell. For example, only the N atoms bonded directly to Ga in $Al_{0.8}Ga_{0.2}N$ gain $0.3e^-$ less electrons than the remaining N atoms. A similar phenomenon is observed for $Al_{0.6}Ga_{0.4}N$, $Al_{0.4}Ga_{0.6}N$, and $Al_{0.2}Ga_{0.8}N$ where the addition of Ga atoms to the unit cell causes more electrons to be transferred from Ga only to specific N atoms, while the charge on the remaining N atoms is constant. This transfer of charge is due to the short-range interactions. For the alloys with a hexagonal structure such as $Al_{0.333}Ga_{0.667}N$ ($1.69e^-$ transferred to N), $Ga_{0.667}In_{0.333}N$ ($1.33e^-$ transferred to N), and $Ga_{0.333}In_{0.667}N$ ($1.28e^-$ transferred to N), the charge trans-

https://dx.doi.org/10.1021/acsami.0c11124
ACS Appl. Mater. Interfaces 2020, 12, 46416−46428

Table 1. Band Gap Values of BN, AlN, GaN, and InN and the Ground-State Configurations of the $Al_{1-x}Ga_xN$ and $Ga_{1-x}In_xN$ Alloys Calculated with PBE, HSE06, SCAN, and G_0W_0 (I for the Indirect Gap and D for the "Minimum Direct" Gap)[a]

structure	PBE (eV)	SCAN (eV)	HSE06 (eV)	BSE (eV)	G_0W_0 (I/D, eV)	E_b (eV)	$E_b^{scaling}$ (eV)
BN	4.67	5.28	5.71	5.49	6.42/7.33	1.84	1.98
AlN	2.92	3.41	4.15	4.02	5.19/5.85	1.83	1.58
$Al_{0.8}Ga_{0.2}N$	2.85	3.28	4.11	3.49	4.90/4.99	1.50	1.35
$Al_{0.6}Ga_{0.4}N$	2.68	3.04	3.96	3.50	4.77/4.89	1.39	1.32
$Al_{0.4}Ga_{0.6}N$	2.51	2.83	3.83	3.45	4.61/4.73	1.28	1.28
$Al_{0.333}Ga_{0.667}N$	2.45	2.78	3.80	3.10	-/4.49	1.39	1.21
$Al_{0.2}Ga_{0.8}N$	2.29	2.57	3.64	3.28	4.37/4.47	1.19	1.21
GaN	2.13	2.37	3.49	3.17	4.11/4.55	1.38	1.23
$Ga_{0.667}In_{0.333}N$	1.37	1.66	2.72	2.37	-/3.19	0.82	0.86
$Ga_{0.333}In_{0.667}N$	0.94	1.13	2.26	2.06	-/2.38	0.32	0.64
InN	0.37	0.64	1.68	1.13	1.30/1.37	0.24	0.37

[a]The energies of the first absorption peak of alloys calculated with GW-BSE (optical gap) are tabulated under the BSE column. Values for exciton binding energy (E_b) calculated with GW-BSE and the model exciton binding energy ($E_b^{scaling}$) obtained from the simple scaling relation for 2D semiconductors[64] are also given.

ferred to N atoms is symmetric because of their atomic arrangements. A full summary of the Bader charge analysis for each atom of each considered structure is given in Table S2.

To be consistent with previous results,[12,15,38] we computed the electronic properties of monolayer BN, AlN, GaN, and InN and went on to compute the electronic properties of the ground-state configurations of $Al_{1-x}Ga_xN$ and $Ga_{1-x}In_xN$ alloys. Figure 3 depicts the electronic band structure, electronic density of states, atom-projected density of states, and BDCD at specific high symmetry points for the valence band and the conduction band of the considered group-III nitride monolayers and ground states of alloyed monolayers calculated with the PBE functional. We see that for hexagonal BN, AlN, GaN, and InN, an indirect band gap is observed with the VBM located at the K high symmetry point, while the CBM is located at the Γ point. We observe that for all of these materials except BN, the VBM is dominated by p_x and p_y orbitals of N, while the CBM of AlN, GaN, and InN is dominated by 2s orbitals of N and p_z orbitals of Al, Ga, and In, respectively. For BN, the VBM is dominated by p_z orbitals of N, and the CBM is dominated by 2s orbitals of N and p_z of B. All four of these structures have localized flat bands from the *M* point to the *K* point in the conduction and valence bands, and the characteristics (orbital contributions) of these localized bands do not change between the two high symmetry points. In addition, these structures have degenerate bands at the highest occupied band at the Γ point, and the orbitals hybridize to form sp^2 sigma bonds.

As depicted in Figure 1, we calculated the band gap of each structure generated by the SQS method using the PBE functional for monolayer $B_{1-x}Al_xN$, $Al_{1-x}Ga_xN$, and $Ga_{1-x}In_xN$ alloys (as indicated in the color axis). As a general trend, the band gap of the $Al_{1-x}Ga_xN$ alloys decrease as Ga concentration increases (from $x = 0$ to $x = 1$), and then, the band gap continues to decrease as In concentration increases in $Ga_{1-x}In_xN$ (again from $x = 0$ to $x = 1$). For the $Al_{1-x}Ga_xN$ distorted hexagonal alloys (at $x = 0.2$, 0.4, 0.6, and 0.8), the modified Brillouin zone (as depicted in Figure 2) extends from the Γ−*K*−*M*−*K*′−*M*′−Γ high symmetry points. For these structures, the band gap is indirect with the VBM at the *K*′ point and the CBM at the Γ point. We also see flat bands between the *K*′ and *M*′ points. $Al_{0.333}Ga_{0.667}N$ is a direct gap material, where the CBM and VBM are located at the Γ point, and because the unit cell is smaller and contains fewer electrons, the density of bands around the CBM and VBM is less than that of the distorted hexagonal $Al_{1-x}Ga_xN$ structures. The energy difference between the Γ and M points of $Al_{0.333}Ga_{0.667}N$ in the valence band is only 0.40 eV, which means that it is a nearly indirect material. The bands around the CBM and VBM for $Al_{0.333}Ga_{0.667}N$ are more parabolic in nature when compared with the flat bands in the other $Al_{1-x}Ga_xN$ structures. This directly affects the effective masses of holes and electrons and therefore thermoelectric properties (as discussed in the foregoing subsections). For these $Al_{1-x}Ga_xN$ monolayers, the VBM is dominated by p_z orbitals of N and the CBM is dominated by 2s orbitals of N and Ga and p_z orbitals of Al. For the $Ga_{0.667}In_{0.333}N$ and $Ga_{0.333}In_{0.667}N$ structures, we observe a direct band gap with the CBM and VBM located at the Γ point with 2s orbitals of N contributing to the VBM and 2s orbitals of N, In, and Ga contributing to the CBM. It is important to note that the only structures which possess a direct band gap are the ones at alloying concentrations of $x = 0.333$ or $x = 0.667$. The distinct band folding associated with these highly symmetric systems (6 atoms per unit cell) could be an explanation for why these structures are direct gap materials. In order to correct the issue of fundamental band gaps being underestimated with PBE, we calculated the band gap of the group-III monolayers and the ground-state configurations of the $Al_{1-x}Ga_xN$ and $Ga_{1-x}In_xN$ alloys using the hybrid functional HSE06 and the SCAN *meta*-GGA functional, as reported in Table 1. We observe that the band gap values calculated with SCAN are slightly higher and follow the same trend as PBE. The band gaps calculated with HSE06 are higher than SCAN and follow the same trend as SCAN and PBE.

Optical Properties. To gain an understanding of the optical properties of these group-III nitride alloys, we performed G_0W_0 calculations on top of PBE functional eigenvalues and wave functions to determine the quasiparticle band gap. Table 1 displays the indirect gap (noted by I) and the "minimum direct gap" for indirect materials (noted by D) calculated with G_0W_0. We see that the G_0W_0 gaps follow the same trend as PBE, SCAN, and HSE06 with the gaps of monolayer $Al_{1-x}Ga_xN$ and $Ga_{1-x}In_xN$ decreasing as sequential alloying concentration increases. To calculate the frequency-dependent dielectric function including electron−electron and electron−hole interactions, we used the G_0W_0 results as a

https://dx.doi.org/10.1021/acsami.0c11124
ACS Appl. Mater. Interfaces 2020, 12, 46416−46428

starting point for the BSE. Figure S2 depicts the imaginary part of the dielectric function calculated with the BSE.

We observe strongly bound excitonic peaks below the quasiparticle band gap for all considered structures from the BSE dielectric function in either the visible or infrared range. This intriguing and applicable property of these monolayer group-III nitride alloys can be understood by the optical band gap and the exciton binding energy. The optical band gap, E_{opt}, is determined by the energy position of the lowest peak in the imaginary part of the dielectric function (indicated by the solid red line in Figure S2 and reported in Table 1), and the exciton binding energy, E_b, is defined as $E_b = E^D_{g,QP} - E_{opt}$, where $E^D_{g,QP}$ is defined as the "minimum direct" quasiparticle gap calculated with G_0W_0 (indicated by the dashed red line in Figure S2). Values of E_b for each structure are given in Figure S2 and reported in Table 1. Our G_0W_0 gap and exciton binding energy results for the nonalloyed monolayers (BN, AlN, GaN, and InN) are in good agreement with previous theoretical results.[38,65] The general trend for the $Al_{1-x}Ga_xN$ and $Ga_{1-x}In_xN$ alloys, with the slight exception of $Al_{0.333}Ga_{0.667}N$, is as alloying concentration increases, the first exciton peak is red-shifted (E_{opt} decreases). This results in a decrease in exciton binding energy as alloying concentration increases. Figure 4, which is created from Table 1, depicts the SCAN,

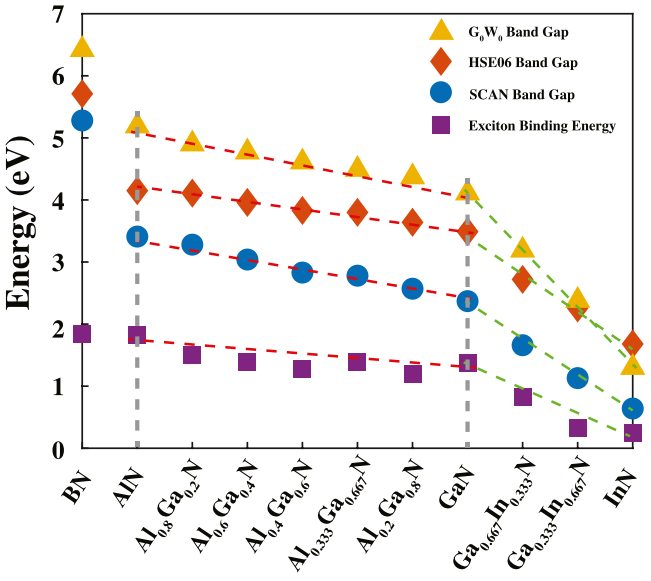

Figure 4. Band gaps calculated with SCAN, HSE06, and G_0W_0 (starting from the PBE functional wave function) in addition to the exciton binding energy as a function of sequential alloying concentration (from Table 1). Linear fits for the $Al_{1-x}Ga_xN$ series are given by the red dotted lines, and linear fits for the $Ga_{1-x}In_xN$ series are given by the green dotted lines. The gray dotted line represents a separation between the different alloy series.

HSE06, G_0W_0, and BSE (optical) band gaps in addition to the exciton binding energies as a function of sequential alloying concentration of all the structures. We observe that for each separate alloy series ($Al_{1-x}Ga_xN$ and $Ga_{1-x}In_xN$), the band gaps and exciton binding energies scale linearly. We fitted each series separately (as seen from the red dotted lines for $Al_{1-x}Ga_xN$ and green dotted lines for $Ga_{1-x}In_xN$), and the equations for the fits (and corresponding R^2 values) are given in Table S3 (including the fit for the BSE-calculated optical gap). This linear band gap behavior with changing concentration has also been reported for bulk group-III nitride alloys.[66] These linear fits give us a more general idea of how the alloying concentration changes the electronic properties and can help predict the band gaps and exciton binding energies of alloys with intermediate concentrations.

The exciton wave function can be expressed in an electron−hole product basis, $\Phi^1 = \sum_{c,v,\vec{k}} A^1_{c,v,\vec{k}} \Phi_{c,\vec{k}} \Phi_{v,\vec{k}}$, where Φ represents an eigenstate in the electron−hole basis, A represents the electron−hole coupling strength, and the summation indexes c, v, and $\vec{k}$ represent the conduction band, valence band, and specific point in reciprocal space (see ref 67). The first eigenstate of the generalized BSE eigenvalue problem (the first exciton peak) can be visualized by plotting $|A^1_{c,v,\vec{k}}|$ as a fat band structure (as previously demonstrated in ref 67). The first peak corresponds to the first bright exciton in the material, which is the result of a direct transition in reciprocal space.[65] Similarly to monolayer TMDs,[36] these group-III nitride alloys can contain multiple bright excitons (depending on alloying concentration). The fat bands (the color axis of Figure 5) of the first bright exciton are plotted on the G_0W_0 band structure and represent the contribution (coupling strength) of the e−h pair at this particular point in reciprocal space. From Figure 5, we observe that all of the direct gap materials have the largest contribution from the e−h pair from the band extrema (VBM and CBM) at the Γ point (smallest direct transition). For the distorted hexagonal phases of $Al_{1-x}Ga_xN$ (x = 0.2, 0.4, 0.6, and 0.8), we see that the coupling strength between the electron and hole is the strongest between the e−h pairs that are around the K'−M' region (the VBM). The energy difference at this specific point (difference between valence and conduction bands) represents the smallest "direct" transition in these indirect semiconductors and arises from the p_z orbitals of N in the valence band in addition to p_z orbitals of Al and Ga and 2s orbitals of N in the conduction band between K' and M' (refer to Figure 3 for more detail). For the indirect nonalloyed monolayers (AlN, GaN, BN, and InN), we see the strongest e−h interactions at the Γ point transition for BN and InN, while we see the strongest interaction at the K point transition for AlN and GaN. In AlN and GaN, this arises from the contribution of p_x and p_y orbitals of N in the valence band in addition to p_x and p_y orbitals of N and p_z orbitals of group-III atoms (Al or Ga) in the conduction band. In contrast, InN and BN have a strong e−h contribution at the Γ point transition. For InN, this stems from the p_x and p_y contribution of N in the valence band and the p_z contribution of In and 2s contribution of N in the conduction band. For BN, the p_x and p_y states for the valence band in addition to the 2s states of N and p_z states of B for the conduction band contribute to the e−h coupling at this Γ point transition.

Because some of these structures contain multiple excitonic peaks (see Fig. S2), we also looked at the fat band structure for the second bright exciton ($|A^2_{c,v,\vec{k}}|$), depicted in Fig. S3. We observe that the second peak for $Al_{0.333}Ga_{0.667}N$ and $Ga_{0.667}In_{0.333}N$ follows the same trend as the first peak. With regard to the distorted hexagonal structures, we see that the e−h contribution is stronger near the Γ point for $Al_{0.8}Ga_{0.2}N$ and $Al_{0.2}Ga_{0.8}N$, while the trend remains the same as $|A^1_{c,v,\vec{k}}|$ for x = 0.4 and x = 0.6. In addition, the second peak of BN has a stronger coupling at the K point transition rather than the Γ point. Being able to exploit the properties of each bright exciton could be a viable route to further engineer optoelectronic devices and an alternative to the widely proposed TMD nanostructures.

https://dx.doi.org/10.1021/acsami.0c11124
ACS Appl. Mater. Interfaces 2020, 12, 46416−46428

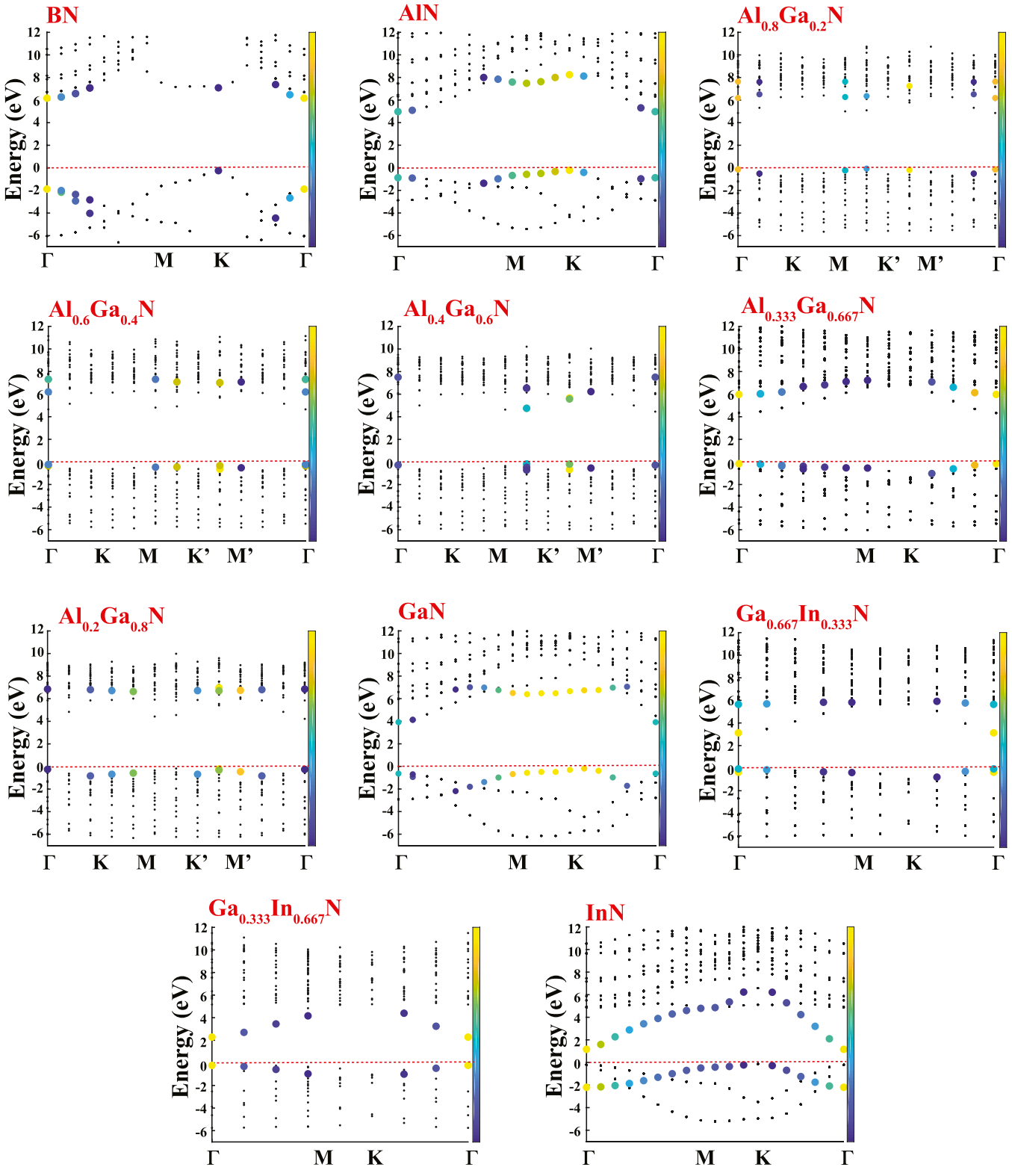

Figure 5. G_0W_0 band structure of each material in the alloy series with the fat bands projected on it. The color represents the contribution of e−h pairs at each point in the Brillouin zone ($|A^{\lambda}_{c,v,\vec{k}}|$) to the first exciton wave function. G_0W_0 and BSE band gaps are also included in Table 1.

It has been reported theoretically that materials with a high quasiparticle gap and a high exciton binding energy (such as 2D h-BN) can be used in polaritonic applications in the ultraviolet (UV) range, where the material can act as a perfect mirror for UV electromagnetic radiation.[65] Some of our considered alloys with a lower quasiparticle gap and lower exciton binding (E_b on the order of 0.5−1.0 eV) can be utilized in the same way monolayer and few-layer TMDs and their heterostructures are utilized. It has been demonstrated theoretically and through experiments that these materials can exhibit electrically driven excitonic light emission and can be used as suitable photovoltaic solar cells, photodetectors, and

https://dx.doi.org/10.1021/acsami.0c11124
ACS Appl. Mater. Interfaces 2020, 12, 46416−46428

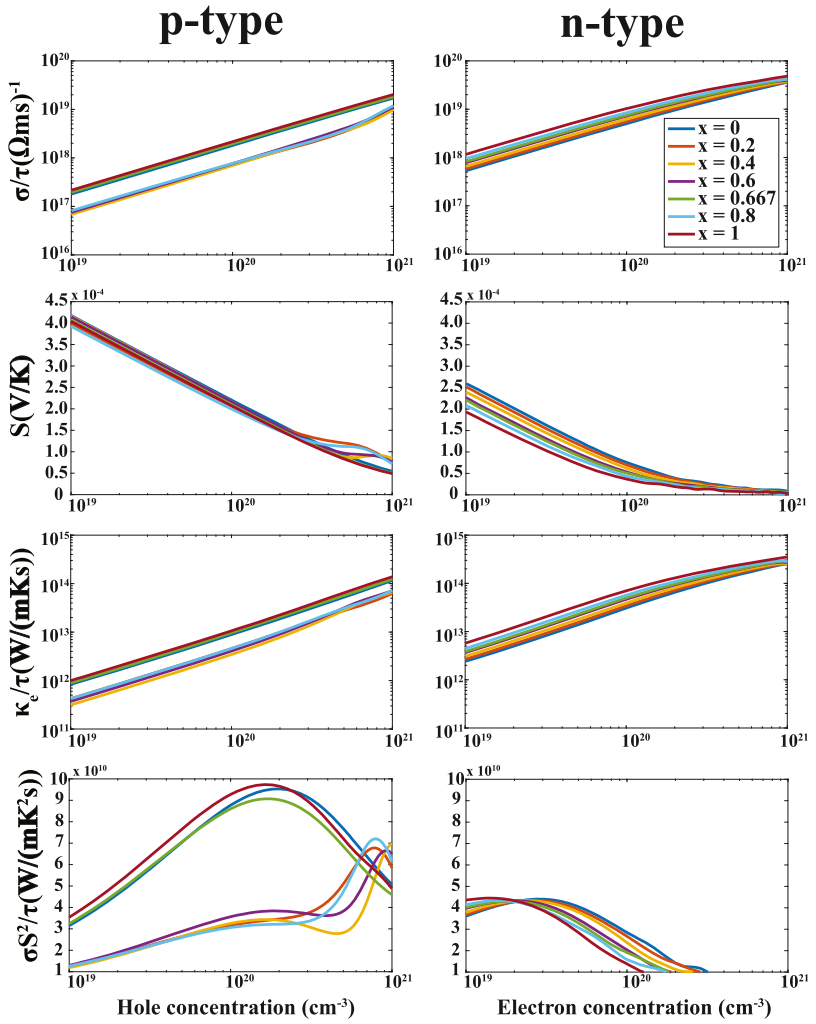

Figure 6. Electrical conductivity (σ), Seebeck coefficient (S), electronic thermal conductivity (κ_e), and power factor (σS^2) as a function of hole concentration (p-type doping) and electron concentration (n-type doping) with respect to a constant relaxation time for AlN and GaN and the ground-state configurations of $Al_{1-x}Ga_xN$ alloys.

valley-optoelectronic devices.[36] Essentially, alloying these group-III monolayers can tune the range at which a device operates, whether it is in the visible light, infrared, or UV.

For excitons in 3D materials, analytic models are sometimes used to describe excitonic behavior and to verify first-principles and experimental results. These excitons can often be modeled by a simple hydrogenic model (Wannier−Mott model). In bulk semiconductors, the expression for exciton binding energy can be given by $E_b^{WM} = 13.6\mu_{reduced}/m_0\varepsilon^2$,[68] where ε is the static dielectric constant, m_0 is the electron mass, and the reduced exciton mass for parabolic bands is defined as $\mu_{reduced} = m_e^* m_h^*/(m_e^* + m_h^*)$. However, the Wannier model does not hold for 2D materials because of the dramatic increase in screening that takes place in 2D structures.[68] Jiang et al.[64] have recently proposed an accurate universal scaling relation between the quasiparticle band gap and exciton binding energy in 2D semiconductors as an alternative to the Wannier−Mott model. This zero intercept, linear scaling relation of $E_b^{scaling} = 0.27E_{g,QP}^D$ is derived from highly accurate GW-BSE calculations and verified using the $k\ p$ method where a universal expression for $E_{g,QP}^D$ in terms of 2D polarizability is established, resulting in the same linear relationship of $E_b^{scaling} \approx E_{g,QP}^D/4$ being analytically obtained.[64] In contrast to the Wannier−Mott model (and other analytic models for excitons that have this dependence[68]), there is no relationship between the effective mass and $E_b^{scaling}$.[64] We used this method to calculate the model exciton binding energy, $E_b^{scaling}$, from our quasiparticle band gaps calculated with G_0W_0, and the values are reported in Table 1. The values of $E_b^{scaling}$ calculated with the scaling relation and the values of E_b calculated with GW-BSE are in good agreement, which adds another level of verification to our exciton binding energy results. To be consistent, we also calculated the exciton binding energy with the Wannier−Mott model (see Table S4). As expected, we observe that using this model results in values of exciton binding that are in worse agreement to our GW-BSE results than the exciton binding calculated with the 2D scaling relation.

Thermoelectric Properties. From the electronic structure calculations based on DFT at the PBE level, we were able to calculate the thermoelectric properties of these structures from Boltzmann transport theory. We specifically calculated the electrical conductivity with respect to the constant relaxation time (σ/τ), the Seebeck coefficient (S), the electronic thermal conductivity with respect to a constant relaxation time (κ_e/τ), and the power factor (σS^2) at varying electron and hole doping concentrations for $Al_{1-x}Ga_xN$ (Figure 6) and $Ga_{1-x}In_xN$ (Figure 7) structures. The effective mass values can give us

https://dx.doi.org/10.1021/acsami.0c11124
ACS Appl. Mater. Interfaces 2020, 12, 46416−46428

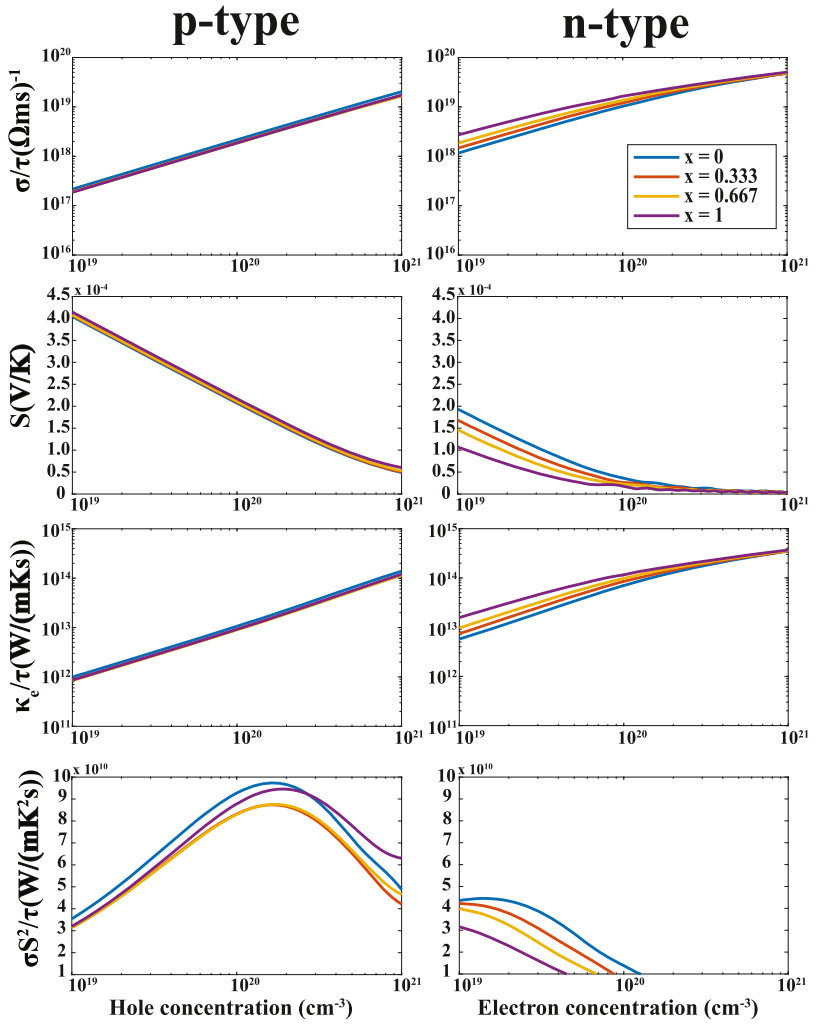

Figure 7. Electrical conductivity (σ), Seebeck coefficient (S), electronic thermal conductivity (κ_e), and power factor (σS^2) as a function of hole concentration (p-type doping) and electron concentration (n-type doping) with respect to a constant relaxation time for GaN and InN and the ground-state configurations of $Ga_{1-x}In_xN$ alloys.

Table 2. Effective Mass for Holes (m_h^*) and Electrons (m_e^*), 2D In-Plane Stiffness Coefficient (C^{2D}), Relaxation Time for Holes (τ_h) and Electrons (τ_e), and Maximum Power Factor for Holes ($PF_{max,h}$) and Electrons ($PF_{max,e}$) Obtained by Multiplying the Peaks of the Bottom Graphs of Figures 6 and 7 ($\sigma S^2/\tau$) by the Appropriate Relaxation Time

structure	<keep-together>m_h^*/m_e^*</keep-together>	C^{2D} (N/m)	τ_h (10^{-14} s)	τ_e (10^{-14} s)	$PF_{max,h}$ (10^{-3} W/mK^2)	$PF_{max,e}$ (10^{-3} W/mK^2)
BN	0.61/1.04	312.9	1.31	0.78	1.19	3.03
AlN	1.30/0.65	186.8	2.0	0.84	1.91	0.37
$Al_{0.8}Ga_{0.2}N$	1.67/0.48	135.7	0.93	0.66	0.82	0.29
$Al_{0.6}Ga_{0.4}N$	1.71/0.49	132.8	0.77	0.48	0.53	0.21
$Al_{0.4}Ga_{0.6}N$	1.77/0.47	132.9	0.66	0.39	0.44	0.17
$Al_{0.333}Ga_{0.667}N$	1.04/0.54	180.8	1.51	0.43	1.37	0.19
$Al_{0.2}Ga_{0.8}N$	1.72/0.42	132.8	0.60	0.35	0.43	0.15
GaN	0.95/0.37	185.9	1.39	0.46	1.35	0.20
$Ga_{0.667}In_{0.333}N$	1.55/0.43	167.7	0.94	0.40	0.82	0.17
$Ga_{0.333}In_{0.667}N$	1.36/0.41	149.4	1.17	0.43	1.02	0.17
InN	1.29/0.13	130.2	1.35	1.38	1.28	0.42

an approximate explanation of why thermoelectric materials perform a certain way. Because of this, we calculated the effective mass of the electrons and holes from the DFT (PBE)-computed band structure of each material by fitting a second-order polynomial to the energy bands at the CBM and VBM (given in Table 2). Expanded methodology is given in the Supporting Information.

For $Al_{1-x}Ga_xN$ structures for p-type doping, the electrical conductivity of $x = 1$ (GaN) is the highest, followed closely by $x = 0$ and $x = 0.667$. The electrical conductivity of the subsequent structures at $x = 0.2$, 0.4, 0.6, and 0.8 is significantly lower, which can be attributed to GaN, AlN, and $Al_{0.333}Ga_{0.667}N$ having a much lower effective hole mass than the other $Al_{1-x}Ga_xN$ alloys because of the presence of more

https://dx.doi.org/10.1021/acsami.0c11124
ACS Appl. Mater. Interfaces 2020, 12, 46416−46428

parabolic bands at the VBM. It is also possible that this low effective mass is associated with the higher symmetry of the AlN, GaN, and $Al_{0.333}Ga_{0.667}N$ structures as opposed to the other distorted hexagonal alloys. The electrical conductivity of the n-type doped $Al_{1-x}Ga_xN$ structures is higher mostly because of the fact that the effective electron mass is much smaller than the effective hole mass. In turn, this also results in Seebeck coefficient values for n-type $Al_{1-x}Ga_xN$ that are around 50% less than p-type $Al_{1-x}Ga_xN$. Consequentially, the power factor of n-type $Al_{1-x}Ga_xN$ structures is much lower than that of the p-type. The highest value for the power factor occurs around a hole concentration of 10^{20} cm^{-3} for GaN, followed closely by $Al_{0.333}Ga_{0.667}N$ and AlN. We also see from Figure 7 that InN, $Ga_{0.333}In_{0.667}N$, and $Ga_{0.667}In_{0.333}N$ have comparable thermoelectric performance to GaN, AlN, and $Al_{0.333}Ga_{0.667}N$ for a hole concentration of 10^{20} cm^{-3}. InN has a significantly low effective electron mass of $0.13m_0$, which can be the reason for the high conductivity, low Seebeck coefficient, and weaker thermoelectric performance for n-type doping. Although the thermal conductivity (which is composed of the electronic thermal conductivity and the lattice thermal conductivity) is not used to calculate the power factor, it is the denominator of the dimensionless figure of merit (ZT). Because of this fact, we calculated the electronic thermal conductivity with respect to the constant relaxation time (κ_e/τ). As expected, κ_e/τ follows almost exactly the same trend as σ/τ (as observed in Figures 6 and 7). Although a more rigorous treatment for the lattice thermal conductivity is required to obtain a full picture of the ZT value of a material, the calculation of the power factor can give us an idea of thermoelectric performance and can approximately be related to the effective electron and hole mass calculated from the DFT band structure.

In order to more rigorously treat the relaxation time and quantify our predictions for power factor, we determined the relaxation time from DPT[62] based on the effective mass approximation. This method has been used successfully to estimate the relaxation time of other 2D materials such as monolayer InSe,[69] and a full description of this methodology can be found in the Supporting Information. Table 2 contains our results for 2D in-plane stiffness coefficients (C^{2D}), DPT-computed hole and electron relaxation times (τ_h and τ_e), and the maximum hole and electron power factors ($PF_{max,h}$ and $PF_{max,e}$). $PF_{max,h}$ and $PF_{max,e}$ are calculated by multiplying the relaxation time by the peak position of the power factor graph (bottom graph of Figures 6 and 7). Our results indicate that when the relaxation time is taken into account, our initial predictions from BoltzTraP2 are still valid, with the same dependence on the effective mass. These relaxation times computed from DPT provide further verification of our transport quantities and observed trends. Our results indicate that changing the alloying concentration in monolayer $Al_{1-x}Ga_xN$ and $Ga_{1-x}In_xN$ can effectively tune the thermoelectric power factor for specific p- and n-type doping concentrations. From the considered alloys, we observe that p-doped $Al_{0.333}Ga_{0.667}N$ has the most potential for device applications because of its high power factor for a large range of hole concentrations, followed closely by p-doped $Ga_{0.667}In_{0.333}N$ and $Ga_{0.333}In_{0.667}N$.

CONCLUSIONS

We have given an in-depth look at the geometric, electronic, optical, and thermoelectric properties of 2D group-III nitrides and their corresponding alloyed structures. First-principles calculations based on the SQS method have revealed energetically stable ground-state structures for $Al_{1-x}Ga_xN$ at x = 0.2, 0.4, 0.6, 0.667, and 0.8 and $Ga_{1-x}In_xN$ at x = 0.333 and 0.667. We see that by increasing the alloying concentration of $Al_{1-x}Ga_xN$ and $Ga_{1-x}In_xN$, the band gap decreases at the PBE, SCAN, HSE06, BSE, and G_0W_0 levels, proving that alloying is an effective way to finely tune the band gap of monolayer group-III nitride materials. Optical properties such as exciton binding energies can be effectively engineered by changing the alloying concentration. We also observe high thermoelectric performance in certain alloys such as p-doped $Al_{0.333}Ga_{0.667}N$ and propose that the thermoelectric performance of these materials is highly dependent on the effective mass obtained from the DFT band structure. We also computed the relaxation time using DPT to further quantify our prediction of thermoelectric properties. The ability to control these properties by varying alloying concentration along with a suitable band gap, high thermoelectric power factor, and strongly bound excitons in the UV, visible, and infrared range make these materials suitable candidates for future electronic, optoelectronic, and thermoelectric devices.

ASSOCIATED CONTENT

Supporting Information

The Supporting Information is available free of charge at https://pubs.acs.org/doi/10.1021/acsami.0c11124.

Vibrational free energy; alloy structural parameters; full Bader charge analysis; band gap linear fits; BSE dielectric function; additional fat bands; Wannier−Mott exciton binding; and thermoelectric and DPT calculation details (PDF)

AUTHOR INFORMATION

Corresponding Author

Can Ataca − *Department of Physics, University of Maryland Baltimore County, Baltimore, Maryland 21250, United States*; Email: ataca@umbc.edu

Authors

Daniel Wines − *Department of Physics, University of Maryland Baltimore County, Baltimore, Maryland 21250, United States*; orcid.org/0000-0003-3855-3754

Fatih Ersan − *Department of Physics, University of Maryland Baltimore County, Baltimore, Maryland 21250, United States; Department of Physics, Aydin Adnan Menderes University, Aydin 09100, Turkey*; orcid.org/0000-0003-0049-105X

Complete contact information is available at: https://pubs.acs.org/10.1021/acsami.0c11124

Notes

The authors declare no competing financial interest.

ACKNOWLEDGMENTS

Part of the calculations have been carried out at the UMBC High Performance Computing Facility (HPCF). This work was supported by the National Science Foundation through Division of Materials Research under the NSF DMR-1726213 Grant.

REFERENCES

(1) Eddy, C. R.; Nepal, N.; Hite, J. K.; Mastro, M. A. Perspectives on Future Directions in III-N Semiconductor Research. *J. Vac. Sci. Technol., A* **2013**, *31*, 058501.

(2) Nakamura, S. Nobel Lecture: Background Story of the Invention of Efficient Blue InGaN Light Emitting Diodes. *Rev. Mod. Phys.* **2015**, *87*, 1139−1151.

(3) Mokkapati, S.; Jagadish, C. III-V Compound SC for Optoelectronic Devices. *Mater. Today* **2009**, *12*, 22−32.

(4) Novoselov, K. S.; Geim, A. K.; Morozov, S. V.; Jiang, D.; Zhang, Y.; Dubonos, S. V.; Grigorieva, I. V.; Firsov, A. A. Electric Field Effect in Atomically Thin Carbon Films. *Science* **2004**, *306*, 666−669.

(5) Zhuang, H. L.; Singh, A. K.; Hennig, R. G. Computational Discovery of Single-layer III-V Materials. *Phys. Rev. B: Condens. Matter Mater. Phys.* **2013**, *87*, 165415.

(6) Durgun, E.; Tongay, S.; Ciraci, S. Silicon and III-V Compound Nanotubes: Structural and Electronic Properties. *Phys. Rev. B: Condens. Matter Mater. Phys.* **2005**, *72*, 075420.

(7) Şahin, H.; Cahangirov, S.; Topsakal, M.; Bekaroglu, E.; Akturk, E.; Senger, R. T.; Ciraci, S. Monolayer Honeycomb Structures of Group-IV Elements and III-V Binary Compounds: First-principles Calculations. *Phys. Rev. B: Condens. Matter Mater. Phys.* **2009**, *80*, 155453.

(8) Auwärter, W.; Suter, H. U.; Sachdev, H.; Greber, T. Synthesis of One Monolayer of Hexagonal Boron Nitride on Ni(111) from B-Trichloroborazine (ClBNH)3. *Chem. Mater.* **2004**, *16*, 343−345.

(9) Mansurov, V.; Malin, T.; Galitsyn, Y.; Zhuravlev, K. Graphene-like AlN Layer Formation on (111)Si Surface by Ammonia Molecular Beam Epitaxy. *J. Cryst. Growth* **2015**, *428*, 93−97.

(10) Tsipas, P.; Kassavetis, S.; Tsoutsou, D.; Xenogiannopoulou, E.; Golias, E.; Giamini, S. A.; Grazianetti, C.; Chiappe, D.; Molle, A.; Fanciulli, M.; Dimoulas, A. Evidence for Graphite-like Hexagonal AlN Nanosheets Epitaxially Grown on Single Crystal Ag(111). *Appl. Phys. Lett.* **2013**, *103*, 251605.

(11) Al Balushi, Z. Y.; Wang, K.; Ghosh, R. K.; Vilá, R. A.; Eichfeld, S. M.; Caldwell, J. D.; Qin, X.; Lin, Y.-C.; DeSario, P. A.; Stone, G.; Subramanian, S.; Paul, D. F.; Wallace, R. M.; Datta, S.; Redwing, J. M.; Robinson, J. A. Two-dimensional Gallium Nitride Realized via Graphene Encapsulation. *Nat. Mater.* **2016**, *15*, 1166−1171.

(12) Kecik, D.; Onen, A.; Konuk, M.; Gürbüz, E.; Ersan, F.; Cahangirov, S.; Aktürk, E.; Durgun, E.; Ciraci, S. Fundamentals, Progress, and Future Directions of Nitride-based Semiconductors and their Composites in Two-dimensional Limit: A First-principles Perspective to Recent Synthesis. *Appl. Phys. Rev.* **2018**, *5*, 011105.

(13) Onen, A.; Kecik, D.; Durgun, E.; Ciraci, S. GaN: From Three- to Two-dimensional Single-layer Crystal and its Multilayer van der Waals Solids. *Phys. Rev. B* **2016**, *93*, 085431.

(14) Bacaksiz, C.; Sahin, H.; Ozaydin, H. D.; Horzum, S.; Senger, R. T.; Peeters, F. M. Hexagonal AlN: Dimensional-crossover-driven Band-gap Transition. *Phys. Rev. B: Condens. Matter Mater. Phys.* **2015**, *91*, 085430.

(15) Huang, Z.; Lü, T.-Y.; Wang, H.-Q.; Yang, S.-W.; Zheng, J.-C. Electronic and Thermoelectric Properties of the Group-III Nitrides (BN, AlN and GaN) Atomic Sheets Under Biaxial Strains. *Comput. Mater. Sci.* **2017**, *130*, 232−241.

(16) Prete, M. S.; Mosca Conte, A.; Gori, P.; Bechstedt, F.; Pulci, O. Tunable Electronic Properties of Two-dimensional Nitrides for Light Harvesting Heterostructures. *Appl. Phys. Lett.* **2017**, *110*, 012103.

(17) Onen, A.; Kecik, D.; Durgun, E.; Ciraci, S. Lateral and Vertical Heterostructures of h-GaN/h-AlN: Electron Confinement, Band Lineup, and Quantum Structures. *J. Phys. Chem. C* **2017**, *121*, 27098−27110.

(18) Onen, A.; Kecik, D.; Durgun, E.; Ciraci, S. In-plane Commensurate GaN/AlN Junctions: Single-layer Composite Structures, Single and Multiple Quantum Wells and Quantum Dots. *Phys. Rev. B* **2017**, *95*, 155435.

(19) Fang, Q.; Huang, Y.; Miao, Y.; Xu, K.; Li, Y.; Ma, F. Interfacial Defect Engineering on Electronic States of Two-Dimensional AlN/MoS_2 Heterostructure. *J. Phys. Chem. C* **2017**, *121*, 6605−6613.

(20) Kadioglu, Y.; Ersan, F.; Kecik, D.; Aktürk, O. Ü.; Aktürk, E.; Ciraci, S. Chemical and Substitutional Doping, and Anti-site and Vacancy Formation in Monolayer AlN and GaN. *Phys. Chem. Chem. Phys.* **2018**, *20*, 16077−16091.

(21) Ahmed, H. M. H.; Benaissa, H.; Zaoui, A.; Ferhat, M. Exploring New Insights in BAlN from Evolutionary Algorithms ab initio Computations. *Phys. Lett. A* **2019**, *383*, 1385−1388.

(22) Wang, V.; Wu, Z. Q.; Kawazoe, Y.; Geng, W. T. Tunable Band Gaps of $In_xGa_{1-x}N$ Alloys: From Bulk to Two-Dimensional Limit. *J. Phys. Chem. C* **2018**, *122*, 6930−6942.

(23) Kanli, M.; Onen, A.; Mogulkoc, A.; Durgun, E. Characterization of Two-dimensional $Ga_{1-x}Al_xN$ Ordered Alloys with Varying Chemical Composition. *Comput. Mater. Sci.* **2019**, *167*, 13−18.

(24) Cai, H.; Chen, B.; Blei, M.; Chang, S. L. Y.; Wu, K.; Zhuang, H.; Tongay, S. Abnormal Band Bowing Effects in Phase Instability Crossover Region of $GaSe_{1-x}Te_x$ Nanomaterials. *Nat. Commun.* **2018**, *9*, 1927.

(25) Yang, S.; Wu, M.; Shen, W.; Huang, L.; Tongay, S.; Wu, K.; Wei, B.; Qin, Y.; Wang, Z.; Jiang, C.; Hu, C. Highly Sensitive Polarization Photodetection Using a Pseudo-One-Dimensional $Nb_{1-x}Ti_xS_3$ Alloy. *ACS Appl. Mater. Interfaces* **2019**, *11*, 3342−3350.

(26) Ersan, F.; Ozaydin, H. D.; Aktürk, E. Influence of Chalcogen Composition on the Structural Transition and on the Electronic and Optical Properties of the Monolayer Titanium Trichalcogenide Ordered Alloys. *Phys. Chem. Chem. Phys.* **2018**, *20*, 1431−1439.

(27) Ersan, F.; Gökoğlu, G.; Aktürk, E. Adsorption and Diffusion of Lithium on Monolayer Transition Metal Dichalcogenides ($MoS_{2(1-x)}Se_{2x}$) Alloys. *J. Phys. Chem. C* **2015**, *119*, 28648−28653.

(28) Beladi-Mousavi, S. M.; Pumera, M. 2D-Pnictogens: alloy-based anode battery materials with ultrahigh cycling stability. *Chem. Soc. Rev.* **2018**, *47*, 6964−6989.

(29) Mo, H.; Zhang, X.; Liu, Y.; Kang, P.; Nan, H.; Gu, X.; Ostrikov, K. K.; Xiao, S. Two-Dimensional Alloying Molybdenum Tin Disulfide Monolayers with Fast Photoresponse. *ACS Appl. Mater. Interfaces* **2019**, *11*, 39077−39087.

(30) Bernardi, M.; Ataca, C.; Palummo, M.; Grossman, J. Optical and Electronic Properties of Two-Dimensional Layered Materials. *Nanophotonics* **2016**, *6*, 479.

(31) Park, S.; Mutz, N.; Schultz, T.; Blumstengel, S.; Han, A.; Aljarb, A.; Li, L.-J.; List-Kratochvil, E. J. W.; Amsalem, P.; Koch, N. Direct Determination of Monolayer MoS_2 and WSe_2 Exciton Binding Energies on Insulating and Metallic Substrates. *2D Materials* **2018**, *5*, 025003.

(32) Bernardi, M.; Palummo, M.; Grossman, J. C. Extraordinary Sunlight Absorption and One Nanometer Thick Photovoltaics Using Two-Dimensional Monolayer Materials. *Nano Lett.* **2013**, *13*, 3664−3670.

(33) Bragança, H.; Riche, F.; Qu, F.; Lopez-Richard, V.; Marques, G. E. Dark-exciton Valley Dynamics in Transition Metal Dichalcogenide Alloy Monolayers. *Sci. Rep.* **2019**, *9*, 4575.

(34) Liu, Y.; Tom, K.; Zhang, X.; Lou, S.; Liu, Y.; Yao, J. Alloying Effect on Bright−Dark Exciton States in Ternary Monolayer $Mo_xW_{1-x}Se_2$. *New J. Phys.* **2017**, *19*, 073018.

(35) Meng, Y.; Wang, T.; Li, Z.; Qin, Y.; Lian, Z.; Chen, Y.; Lucking, M. C.; Beach, K.; Taniguchi, T.; Watanabe, K.; Tongay, S.; Song, F.; Terrones, H.; Shi, S.-F. Excitonic Complexes and Emerging Interlayer Electron−Phonon Coupling in BN Encapsulated Monolayer Semiconductor Alloy: $WS_{0.6}Se_{1.4}$. *Nano Lett.* **2019**, *19*, 299−307.

(36) Mueller, T.; Malic, E. Exciton Physics and Device Application of Two-dimensional Transition Metal Dichalcogenide Semiconductors. *npj 2D Mater. Appl.* **2018**, *2*, 29.

(37) Arnaud, B.; Lebègue, S.; Rabiller, P.; Alouani, M. Huge Excitonic Effects in Layered Hexagonal Boron Nitride. *Phys. Rev. Lett.* **2006**, *96*, 026402.

(38) Prete, M. S.; Grassano, D.; Pulci, O.; Kupchak, I.; Olevano, V.; Bechstedt, F. Giant Excitonic Absorption and Emission in Two-dimensional Group-III Nitrides. *Sci. Rep.* **2020**, *10*, 10719.

(39) Zheng, J.-c. Recent Advances on Thermoelectric Materials. *Front. Phys. China* **2008**, *3*, 269−279.

https://dx.doi.org/10.1021/acsami.0c11124
ACS Appl. Mater. Interfaces 2020, 12, 46416−46428

(40) Sztein, A.; Ohta, H.; Sonoda, J.; Ramu, A.; Bowers, J. E.; DenBaars, S. P.; Nakamura, S. GaN-Based Integrated Lateral Thermoelectric Device for Micro-Power Generation. *Appl. Phys. Express* **2009**, *2*, 111003.
(41) Sztein, A.; Haberstroh, J.; Bowers, J. E.; DenBaars, S. P.; Nakamura, S. Calculated Thermoelectric Properties of $In_xGa_{1-x}N$, $In_xAl_{1-x}N$, and $Al_xGa_{1-x}N$. *J. Appl. Phys.* **2013**, *113*, 183707.
(42) Karaaslan, Y.; Yapicioglu, H.; Sevik, C. Assessment of Thermal Transport Properties of Group-III Nitrides: A Classical Molecular Dynamics Study with Transferable Tersoff-Type Interatomic Potentials. *Phys. Rev. Appl.* **2020**, *13*, 034027.
(43) Kaur, P.; Bera, C. Effect of Alloying on Thermal Conductivity and Thermoelectric Properties of CoAsS and CoSbS. *Phys. Chem. Chem. Phys.* **2017**, *19*, 24928−24933.
(44) Du, Z.; Chen, X.; Zhu, J.; Cui, J. Effect of Ga Alloying on Thermoelectric Properties of InSb. *Curr. Appl. Phys.* **2018**, *18*, 893−897.
(45) Zunger, A.; Wei, S.-H.; Ferreira, L. G.; Bernard, J. E. Special Quasirandom Structures. *Phys. Rev. Lett.* **1990**, *65*, 353−356.
(46) Wei, S.-H.; Ferreira, L. G.; Bernard, J. E.; Zunger, A. Electronic Properties of Random Alloys: Special Quasirandom Structures. *Phys. Rev. B: Condens. Matter Mater. Phys.* **1990**, *42*, 9622−9649.
(47) van de Walle, A.; Tiwary, P.; de Jong, M.; Olmsted, D. L.; Asta, M.; Dick, A.; Shin, D.; Wang, Y.; Chen, L.-Q.; Liu, Z.-K. Efficient Stochastic Generation of Special Quasirandom Structures. *Calphad* **2013**, *42*, 13−18.
(48) Blöchl, P. E. Projector Augmented-wave Method. *Phys. Rev. B: Condens. Matter Mater. Phys.* **1994**, *50*, 17953−17979.
(49) Perdew, J. P.; Burke, K.; Ernzerhof, M. Generalized Gradient Approximation Made Simple. *Phys. Rev. Lett.* **1996**, *77*, 3865−3868.
(50) Grimme, S. Semiempirical GGA-type Density Functional Constructed with a Long-range Dispersion Correction. *J. Comput. Chem.* **2006**, *27*, 1787−1799.
(51) Monkhorst, H. J.; Pack, J. D. Special Points for Brillouin-zone Integrations. *Phys. Rev. B: Solid State* **1976**, *13*, 5188−5192.
(52) Kresse, G.; Furthmüller, J. Efficient Iterative Schemes for ab initio Total-energy Calculations using a Plane-wave Basis Set. *Phys. Rev. B: Condens. Matter Mater. Phys.* **1996**, *54*, 11169−11186.
(53) Heyd, J.; Scuseria, G. E.; Ernzerhof, M. Hybrid Functionals based on a Screened Coulomb Potential. *J. Chem. Phys.* **2003**, *118*, 8207−8215.
(54) Sun, J.; Ruzsinszky, A.; Perdew, J. P. Strongly Constrained and Appropriately Normed Semilocal Density Functional. *Phys. Rev. Lett.* **2015**, *115*, 036402.
(55) van de Walle, A. Multicomponent Multisublattice Alloys, Nonconfigurational Entropy and other Additions to the Alloy Theoretic Automated Toolkit. *Calphad* **2009**, *33*, 266−278.
(56) Henkelman, G.; Arnaldsson, A.; Jónsson, H. A Fast and Robust Algorithm for Bader Decomposition of Charge Density. *Comput. Mater. Sci.* **2006**, *36*, 354−360.
(57) Hybertsen, M. S.; Louie, S. G. Electron Correlation in Semiconductors and Insulators: Band Gaps and Quasiparticle Energies. *Phys. Rev. B: Condens. Matter Mater. Phys.* **1986**, *34*, 5390−5413.
(58) Hedin, L. New Method for Calculating the One-Particle Green's Function with Application to the Electron-Gas Problem. *Phys. Rev.* **1965**, *139*, A796−A823.
(59) Onida, G.; Reining, L.; Rubio, A. Electronic Excitations: Density-functional Versus Many-body Green's-function Approaches. *Rev. Mod. Phys.* **2002**, *74*, 601−659.
(60) Dancoff, S. M. Non-Adiabatic Meson Theory of Nuclear Forces. *Phys. Rev.* **1950**, *78*, 382−385.
(61) Madsen, G. K. H.; Carrete, J.; Verstraete, M. J. BoltzTraP2, a Program for Interpolating Band Structures and Calculating Semi-classical Transport Coefficients. *Comput. Phys. Commun.* **2018**, *231*, 140−145.
(62) Bardeen, J.; Shockley, W. Deformation Potentials and Mobilities in Non-Polar Crystals. *Phys. Rev.* **1950**, *80*, 72−80.
(63) Togo, A.; Tanaka, I. First principles Phonon Calculations in Materials Science. *Scr. Mater.* **2015**, *108*, 1−5.
(64) Jiang, Z.; Liu, Z.; Li, Y.; Duan, W. Scaling Universality between Band Gap and Exciton Binding Energy of Two-dimensional Semiconductors. *Phys. Rev. Lett.* **2017**, *118*, 266401.
(65) Ferreira, F.; Chaves, A. J.; Peres, N. M. R.; Ribeiro, R. M. Excitons in Hexagonal Boron Nitride Single-layer: A New Platform for Polaritonics in the Ultraviolet. *J. Opt. Soc. Am. B* **2019**, *36*, 674−683.
(66) Wu, J.; Walukiewicz, W.; Yu, K. M.; Ager, J. W.; Li, S. X.; Haller, E. E.; Lu, H.; Schaff, W. J. Universal Bandgap Bowing in Group-III Nitride Alloys. *Solid State Commun.* **2003**, *127*, 411−414.
(67) Bokdam, M.; Sander, T.; Stroppa, A.; Picozzi, S.; Sarma, D. D.; Franchini, C.; Kresse, G. Role of Polar Phonons in the Photo Excited State of Metal Halide Perovskites. *Sci. Rep.* **2016**, *6*, 28618.
(68) Ramasubramaniam, A. Large Excitonic Effects in Monolayers of Molybdenum and Tungsten dichalcogenides. *Phys. Rev. B: Condens. Matter Mater. Phys.* **2012**, *86*, 115409.
(69) Sprague, L. W.; Huang, C.; Song, J.-P.; Rubenstein, B. M. Maximizing Thermoelectric Figures of Merit by Uniaxially Straining Indium Selenide. *J. Phys. Chem. C* **2019**, *123*, 25437−25447.

https://dx.doi.org/10.1021/acsami.0c11124
ACS Appl. Mater. Interfaces 2020, 12, 46416−46428